BJRS
BRAZILIAN JOURNAL OF RADIATION SCIENCES

doi.org/10.15392/2319-0612.2026.3031
Braz. J. Radiat. Sci., Rio de Janeiro
2026, 14(2) | 01-26 | e3031
Editor: Prof. Dr. Bernardo Maranhão Dantas
Editor: Prof. Dr. Alfredo Lopes Ferreira Filho
Submitted: 2025-11-12
Accepted: 2026-01-05

Original Article

Monte Carlo simulations study of non-collinear gamma-ray cascade correlation emissions for medical imaging

Nkuba[a*], L. L.; Lugendo[b], I. J.

[a] Nuclear Technology and Technical Services Directorate, Tanzania Atomic Energy Commission, P.O. Box 1585, Block AF, Plot No. 634, Atomu Road, Mnadani Street, Kikombo Area, 41206, Dodoma, Tanzania.
[b] Department of Physics, University of Dar es Salaam, Physics Building, Uvumbuzi Road, P.O. Box 35063, Dar es Salaam, Tanzania.

*Correspondence: leonid_nkuba@yahoo.co.uk

Abstract: Conventional imaging techniques such as SPECT and PET cannot directly identify the positions of individual decaying nuclei. As such, they heavily rely on statistical backprojection for image point reconstruction. Therefore, this study explores an alternative approach using non-collinear gamma-ray cascade emissions, which are emitted directly from the decay position and unaffected by positron movement. Detecting these cascades in coincidence allows precise localization of decay events, enabling direct image point reconstruction. To evaluate this concept, GATE Monte Carlo simulation was used to simulate the cascade emission from ^{111}In-ion point sources and detection using collimated small animal PET scanner. Finally, a custom image reconstruction algorithm was developed to estimate the three-dimensional position of a decaying nucleus by calculating the midpoint of the shortest segment, or the intersection, between two collimator projections from a valid coincidence event. The results show that at the center of the field of view, image sensitivities of 22.2 cps/MBq in air and 20.0 cps/MBq in a PMMA phantom were achieved. Furthermore, a spatial resolution of 4.1 mm FWHM was obtained in the transaxial direction and 7.6 mm FWHM in the axial direction. The imaging system is capable of resolving two-point sources separated by 8.0 mm (transaxial) and 10.0 mm (axial). The results from this simulation study indicate that the proposed imager with its image reconstruction method surpasses conventional PET and SPECT in emission point localization accuracy.

Keywords: Medical image reconstruction, non-collinear gamma ray, 3D source location, GATE Monte Carlo simulation.

doi.org/10.15392/2319-0612.2026.3031
Braz. J. Radiat. Sci., Rio de Janeiro
2026, 14(2) | 01-26| e3031
Editor: Prof. Dr. Bernardo Maranhão Dantas
Editor: Prof. Dr. Alfredo Lopes Ferreira Filho
Submitted: 2025-11-12
Accepted: 2026-01-05

Estudo por simulações de Monte Carlo das emissões correlacionadas em cascata de raios gama não colineares para imageamento médico

Resumo: Técnicas de imagem convencionais, como SPECT e PET, não conseguem identificar diretamente as posições dos núcleos individuais em decaimento. Por esse motivo, dependem fortemente da retroprojeção estatística para a reconstrução dos pontos de imagem. Assim, este estudo explora uma abordagem alternativa baseada em emissões em cascata de raios gama não colineares, que são emitidas diretamente a partir da posição de decaimento e não são afetadas pelo movimento do pósitron. A detecção dessas cascatas em coincidência permite a localização precisa dos eventos de decaimento, possibilitando a reconstrução direta dos pontos de imagem. Para avaliar esse conceito, utilizou-se a simulação Monte Carlo GATE para simular a emissão em cascata de fontes pontuais de ^{111}In e a detecção por meio de um scanner PET colimado para pequenos animais. Por fim, foi desenvolvido um algoritmo personalizado de reconstrução de imagem para estimar a posição tridimensional de um núcleo em decaimento, calculando o ponto médio do menor segmento — ou a interseção — entre duas projeções de colimador provenientes de um evento de coincidência válido. Os resultados mostram que, no centro do campo de visão, foram alcançadas sensibilidades de imagem de 22,2 cps/MBq no ar e 20,0 cps/MBq em um fantoma de PMMA. Além disso, foram obtidas resoluções espaciais de 4,1 mm FWHM na direção transaxial e 7,6 mm FWHM na direção axial. O sistema de imagem foi capaz de resolver duas fontes pontuais separadas por 8,0 mm (transaxial) e 10,0 mm (axial). Os resultados desta simulação indicam que o dispositivo de imagem proposto, juntamente com seu método de reconstrução, supera as técnicas convencionais de PET e SPECT em termos de precisão na localização do ponto de emissão.

Palavras-chave: Reconstrução de imagem médica, raio gama não colinear, localização 3D da fonte, simulação Monte Carlo GATE.

1. INTRODUCTION

Single photon emission computed tomography (SPECT) and positron emission tomography (PET) are commonly used imaging modalities in nuclear medicine. Despite their widespread clinical uses, both PET and SPECT are not capable of locating individual decaying nuclei [1, 2]. In the case of SPECT, the information is limited to the direction of the photon along a collimation axis. While PET provides a straight line-of-response (LoR) between the two detectors registering a coincidence pair. Thus, neither modality can determine the location of an individual decaying nucleus. These limitations necessitate statistical backprojection techniques to reconstruct an image.

Furthermore, in a PET imaging system, the annihilation point may not correspond to the decay vertex of the nucleus due to the random motion of positrons, and therefore the point of gamma emission. The reconstructed LoR, thus, may not overlap with the tumor location and would blur the image. Recently, the time-of-flight (TOF) PET has been developed, and due to its high time resolution [3, 4, 5], the position of a positron can be estimated at a higher resolution, and not only along a line as in conventional PET [3, 6]. However, the position of an individual decaying nucleus still cannot be located due to random positron movement.

Several studies identify this issue, and many solutions have been proposed and others are being experimented [2, 7, 8]. It has been proposed that medical imaging by the non-collinear gamma-ray cascade decay with collimated detectors is likely a promising way to overcome the stated limitations in conventional PET and SPECT for at least two reasons [9]: event-by-event analysis determines the decay vertices of nuclei and the emissions are devoid of blurring from random positron motions [1, 10]. The proposed method is reported to improve signal-to-background ratio [7], and more specifically by a factor of more than 3 compared to that of conventional SPECT imaging systems [11].

Several radio-isotopes decay through the emission of cascade gamma rays. Some of these radio-isotopes are already being used in nuclear medicine and other are still under research. The cascade gamma rays from these radio-isotopes can be detected in coincidence and used to create coincident event-based images. By detecting cascade-emitted photons in coincidence with angular-resolving detectors, the source position can be localized through the intersection of their trajectories. Angular resolution can be achieved using either Compton imaging or mechanical collimation [11, 12].

While several groups have taken the advantage of cascade gamma-rays in creating coincident-based images [7, 8, 10, 13 - 20], the idea of producing coincidence-based images from cascade gamma-rays using a collimated PET scanner has not been explored. It is a well-known feature of some radioactive isotopes with cascade gamma-rays that their angular correlations are non-collinear [1, 21]. Thus, a coincidence detection of a non-collinear cascade pair, with the same electronic arrangement as in PET, but with an additional retrofit of a physical collimator as in SPECT imaging assembly, will yield a three-dimensional (3D) decay vertex of each nucleus. Usually, through finding an intersection point or mid-point of the shortest segment between two non-collinear collimator projections, a 3D vertex (image point) of a decaying nucleus can be found [8, 18].

Indium-111 (^{111}In) isotope with a 2.83 days physical half-life has been identified as a good test candidate. ^{111}In decays by electron capture (99.99%) to ^{111}Cd, emitting a strong gamma ray cascade pair of 171.3 keV (90.61% yield) and 245.4 keV (94.12% yield), with 85 ns as the half-life of the intermediate state of the cascade emission [18, 22]. The two major emitted gamma-rays are resolved and exhibit high yield. These features make ^{111}In an ideal tracer for the diagnosis and assessment of many health disorders [23, 24].

To explore the idea of using physically collimated small animal PET as a prototype to produce coincidence-based images from the non-collinear cascade gamma-ray emissions of ^{111}In isotope, a Geant4 Application for Tomographic Emission (GATE) Monte Carlo simulation was used to simulate the emission and detection of cascade gamma-ray using a

small animal PET instrument of pixelated gadolinium orthosilicate (GSO) detectors [9]. GATE is an open-source software dedicated to image simulation (SPECT, PET, CT, and optics) and radiotherapy [25]. The analysis of GATE simulations were performed using a written C++ file executed through root software [26].

2. MATERIALS AND METHODS

2.1. Small animal PET imaging system

A small animal PET imaging system of RIKEN used in this study has been described in detail elsewhere [9, 27, 28 - 31]. The aforementioned small animal PET assembly is mainly used for research purposes. Its geometric characteristics and detector material composition are given in Table 1.

Table 1: The geometric characteristic of a RIKEN small animal PET assembly

ITEMS	DESCRIPTION
Detector material	GSO (Ce)
Dimensions of the Lower/First layer of crystals (mm^3)	1.6 × 2.4 × 7
Dimensions of the Upper/Second layer of crystals (mm^3)	1.6 × 2.4 × 8
Crystal Array	11 × 15
Crystal pitch (mm)	1.7 × 2.5
Number of crystals per detector (module)	165
Number of detectors (modules) in the system	16
The outer diameter of the prototype (mm)	130
The inner diameter of the prototype (mm)	95
Axial field of view (mm)	37.5

2.2. The model of a small animal PET imaging system with collimators

Figures 1(a) and 1(b) show a photo of a RIKEN PET and the GATE simulation of RIKEN PET, respectively. In the GATE digitization module, 0.549 ns was used as the time resolution of the Gadolinium Orthosilicate (GSO) crystal [32]. The time resolution is defined

by how accurately the time at which a photon crossed the detector can be determined. Based on the geometry of the RIKEN PET assembly, a trapezoidal-shaped collimator geometry was designed [31]. Figure 1(c) and (d) shows the GATE simulated model of the RIKEN PET assembly to which the collimators are attached.

Figure 1: RIKEN PET assembly. (a) A photo of the PET system [28], (b) GATE model of the PET system, (c) and (d) GATE model of the PET system with collimators (in blue) attached.

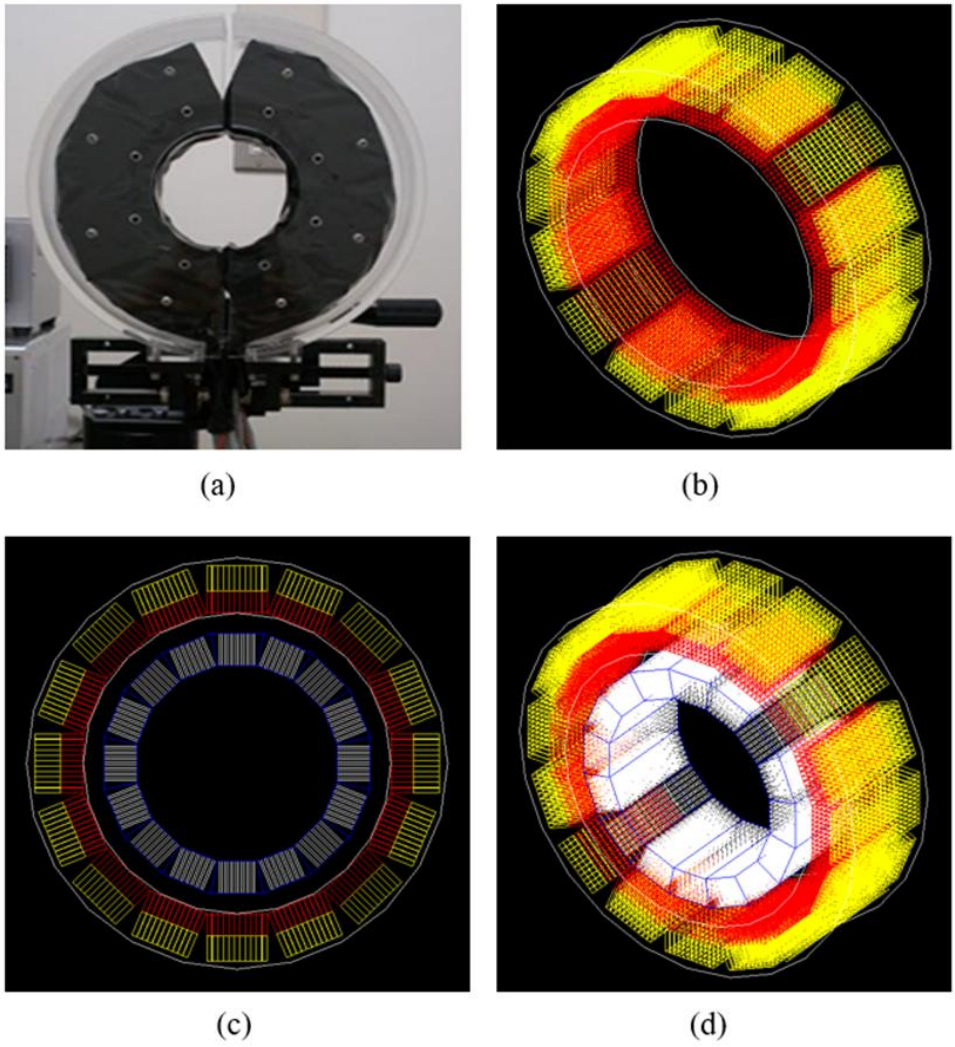

As shown in Figures 1 (c) and (d), the collimation system is made of 16 trapezoidal collimator blocks (in blue), making a polygonal ring with an outer minimum radius of 41 mm. With the trade-off between geometrical acceptances, photon leaking via septa walls, and spatial resolution in mind, a septa thickness of 1.0 mm was used.

Because of its high stopping power, pure tungsten (W) with a density of approximately 19.3 g/cm^3, was chosen and simulated as collimator material over Lead and other commonly used collimator materials. The simulated single collimator block had dimensions of 16.31 mm × 37.5 mm for the surface-facing crystals and dimensions of 12.33 mm × 37.5 mm for the surface-facing scanned object [31]. The thickness of the collimator (hole length) was limited to 10 mm to avoid overlapping of neighboring collimator blocks. A single collimator block consists of 105 holes (1.5 × 0.7) mm [31]. The collimator holes are centered on the crystals, with a 7×15 array as shown in Figure 2.

Figure 2: The view of a single PET module fitted with one of the collimator designs within GATE. The detector crystals (yellow) are 2.4 mm × 1.6 mm, separated by 0.1 mm reflectors. The trapezoidal collimator outline (blue) encloses the collimator holes (white).

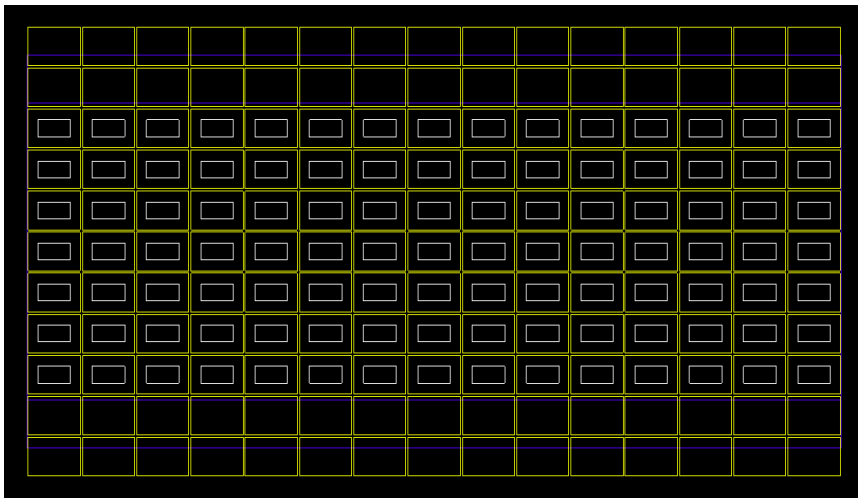

2.3. Radioactive source modeling and simulations

In this study, for coincidence based images and their imaging parameters, a ^{111}In ion point-like source with a diameter of 0.25 mm and an activity of 2.0 MBq was simulated for 900 s (Figure 3). The full radioactive decay of ^{111}In, which includes the emission of 171.3 keV and 245.4 keV gamma rays and an intermediate half-life of 85 ns [8, 18], was incorporated into the simulation.

Figure 3: GATE simulation of a collimated PET detector, with phantom and a decaying source.

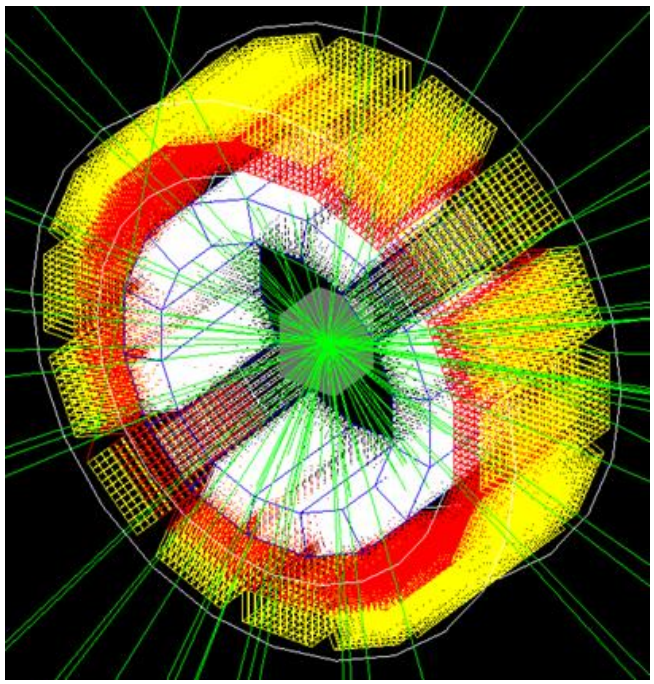

However, for testing if the source was modelled and simulated correctly, through assessing the curve if it portray an exponential decay, as well as evaluating the lifetime between cascade photons, an ^{111}In-ion point-like source with 1.0 MBq and a diameter of 0.25 mm was simulated for 100 s at the center of the field of view (FoV) of an uncollimated small animal PET scanner.

2.4. Image reconstruction algorithm and imaging parameters

2.4.1. Image reconstruction algorithm

As described by [31], the image reconstruction algorithm consists of several steps. First step is to detect two gamma-rays from a single cascade pair in coincidence, second is to construct two non-collinear lines stemming from interaction positions (P1 and P2), which passes through the collimator holes (collimator projections), resembling to SPECT acquisition. The last step, is to determine the intersection point or mid-point of the shortest segment between the two non-collinear lines. If the two non-collinear lines (in red), which are defined normal to the detector crystal face, are very close to each other but do not

intersect (skew) as shown in Figure 4, then a 3D decay vertex is then computed as the mid-point located on the shortest segment between the two skew lines. However, if the lines intersect, the intersection point between the two lines determine a 3D decay vertex of individual nucleus. As shown in Figure 4, the mild-point formula was used to solve for 3D vertex in both skew and intersecting lines conditions. However, this algorithm is not valid for parallel detector orientation (180^{o} detector orientation).

Figure 4: Illustration of image reconstruction algorithm and procedure. The light blue dashed lines emitted from the source to P1 and P2 represent the 171 keV and 245 keV gamma-rays, respectively [8, 31].

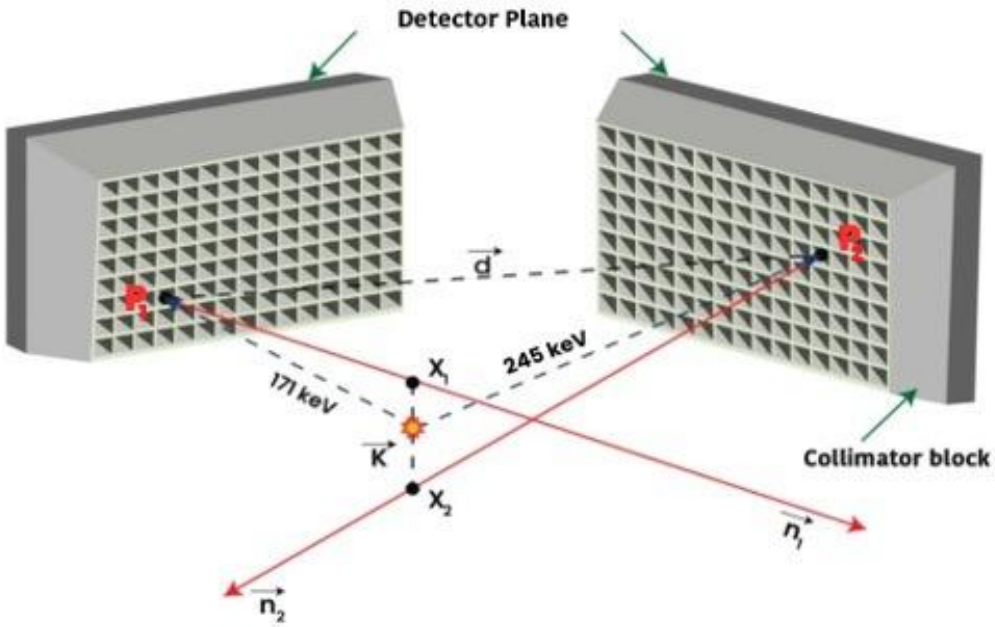

Therefore, with an optimal collimation system, radioisotope distribution that emits the non-collinear gamma-rays in cascade is then assembled by the intersections of the lines, which are 3D points. These 3D points are regarded as small volumes of radioisotope distribution. Finally, the whole image, which is the representation of radioactivity distribution in the scanned object, is then reconstructed from all the small volumes binned together. The algorithm has been designed to accept gamma-ray energies of 171.3 keV ± 15% and 245.4 keV ± 15%. Also the two single events must be detected within a set time coincidence window of 100 ns. A detailed description of the coincidence detection of the non-collinear gamma-rays cascade and the image reconstruction algorithm can be found elsewhere [8, 31].

2.5. Coincidence event-based images

i) Image sensitivity

The image sensitivity, which is quantified as the number of useful detected coincidence photons per second relative to the amount of radioactivity in the scanner (cps/MBq) was determined with a 0.25 mm diameter, 2.0 MBq ^{111}In-ion point-like source in air and then in a cubic (10 × 10 × 10 mm) polymethyl methacrylate (PMMA) phantom as scattering medium. In all cases, the source was located at the center of the FoV. The acquisition time was 900 s, whereby a total of 1.8×10^9 decays was simulated and transported. Finally, valid coincidence events in all detector orientations (except for parallel detectors) were used to reconstruct the two-dimension (2D) images and estimation of sensitivity.

ii) Spatial resolution and image size

To determine the spatial resolution and estimation of image size, five-point sources of 0.25 mm, 1.0 mm, 2.0 mm, 4.0 mm, and 8.0 mm diameter each, containing 0.4 MBq, 2.0 MBq, 3.0 MBq, 5.0 MBq, and 7.0 MBq each, were simulated in the air at the center of FoV for 900 s each. The one-dimension (1D) projections acquired from each direction (x, y, and z) were plotted into histograms, and followed by fitting to a Gaussian function to obtain the sigma value (σ). The spatial resolution in terms of full width at half maximum (FWHM) was calculated as shown in Equation (01). The simulation data for the point source in PMMA phantom given in part (i) were used to determine the effects of scatter on spatial resolution. The FWHM (mm) values were used as an estimate of the size of the reconstructed images in the transaxial direction (x-axis and y-axis) and axial direction (z-axis).

$$FWHM = 2.35482 \times \sigma \quad (01)$$

Where the FWHM is the calculated spatial resolution and σ is the standard deviation

iii) Resolving power

To determine the resolving power of the prototype imager, two-point-like sources each with 0.25 mm diameter and 2.0 MBq in a PMMA phantom, were simulated close to each other, at 1.0 mm, 2.0 mm, 3.0 mm, 4.0 mm, 5.0 mm, 6.0 mm, 7.0 mm, 8.0 mm, 9.0 mm

and 10 mm distances between centers of the point sources in transaxial and axial directions. Each phantom with its point sources was simulated separately for 900 s. The 2D flattened images as well as their 1D projection profiles were used to estimate the resolving power of the simulated imager.

3. RESULTS AND DISCUSSIONS

3.1. Validation of ^{111}In source modeling and simulation

i) Decay exponential curve

The coincidence events were extracted using a 100 ns time coincidence window. Subsequently, the timing plots (time2 - time1) of the coincidences under three different conditions were analyzed.

Firstly condition, with no cut – to show the total acquired coincidence events: Coincidences->Draw ("time2-time1",""). The timing plot shows a total of 7,247,942 coincidences. However, no exponential decay is evident (see Figure 5). Secondly, a simple energy cut to the timing plot (time2-time1): Coincidences->Draw ("time2-time1", "energy1+energy2>0.280"), was applied to reveal true coincidences after removing crystal-crystal scatters. It appears more like an exponential decay (see Figure 6), but there is still a significant amount of background due to recorded low-energy accidentals.

Figure 5: Timing plots (time2-time1) of coincidences acquired through simulation of a full radioactive decay of ^{111}In-ion point-like source : With no cut.

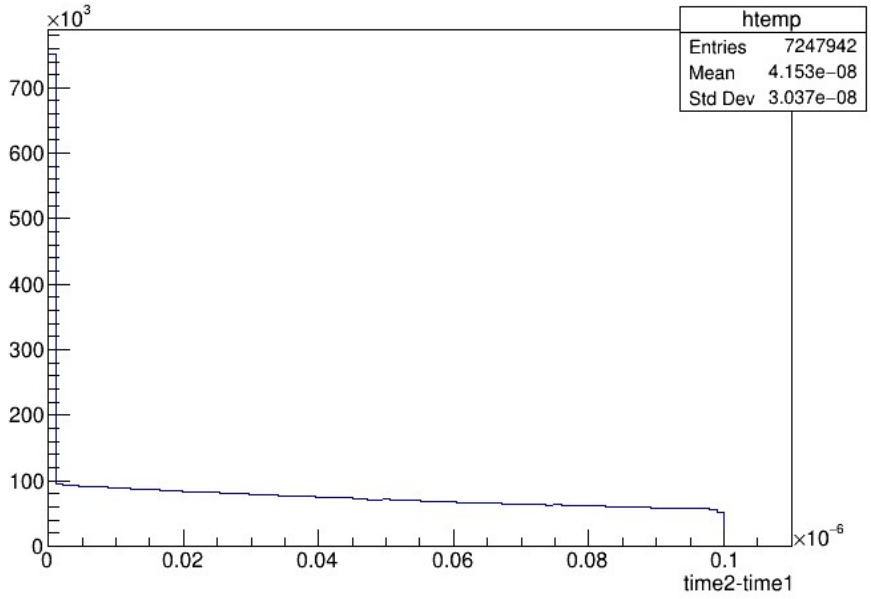

Figure 6: Timing plots (time2-time1) of coincidences acquired through simulation of a full radioactive decay of ^{111}In-ion point-like source : With simple energy cut.

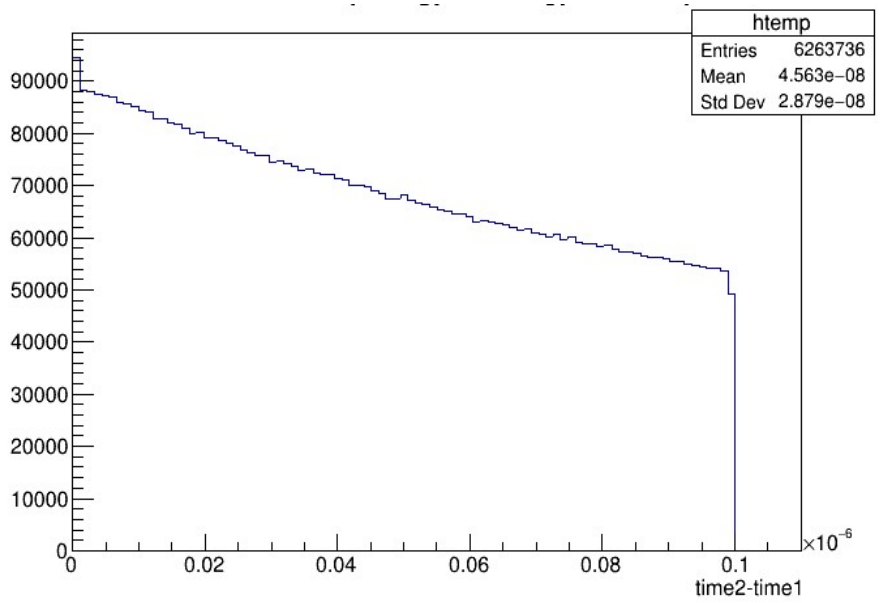

Thirdly, to reveal only the true coincidences, both the energy cut and the true events cut: Coincidences-> Draw ("time2-time1", "energy1+energy2>0.280 && eventID1 == eventID2") were applied to the timing plot (time2 - time1). As shown in Figure 7, an exponential decay is evident as expected.

Figure 7: Timing plots (time2-time1) of coincidences acquired through simulation of a full radioactive decay of ^{111}In-ion point-like source : With both the energy cut and the true events cut.

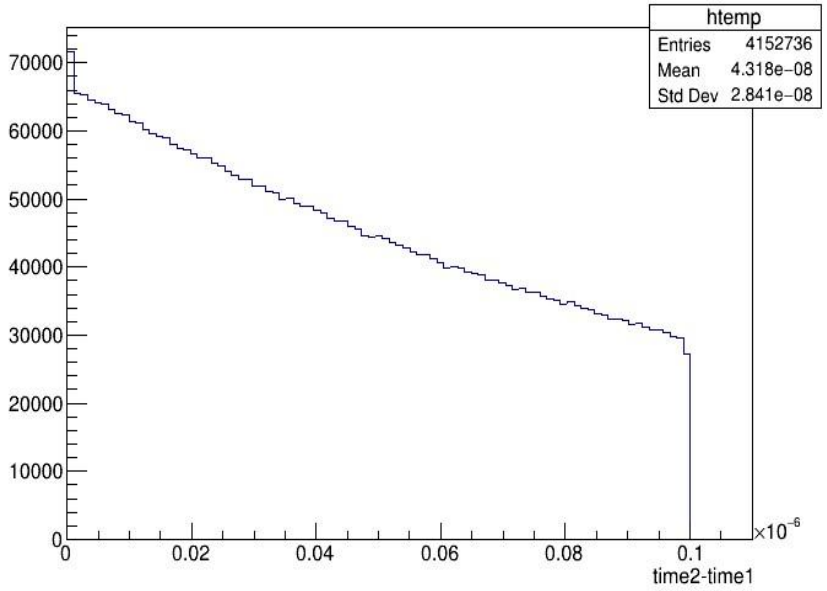

ii) The 85 ns lifetime between 171.3 keV and 245.4 keV

To verify that the lifetime between 171.3 keV and 245.4 keV was correctly modelled in GATE simulations, the timing plots (time2-time1) with energy cuts and true coincidence event cuts, as shown in Figure 6, were fitted to an exponential function in ROOT, as illustrated in Figure 8. The fitting results are provided in Table 2.

Figure 8: Timing plot (time2-time1) of true coincidence events for a full radioactive decay fitted with exponential function.

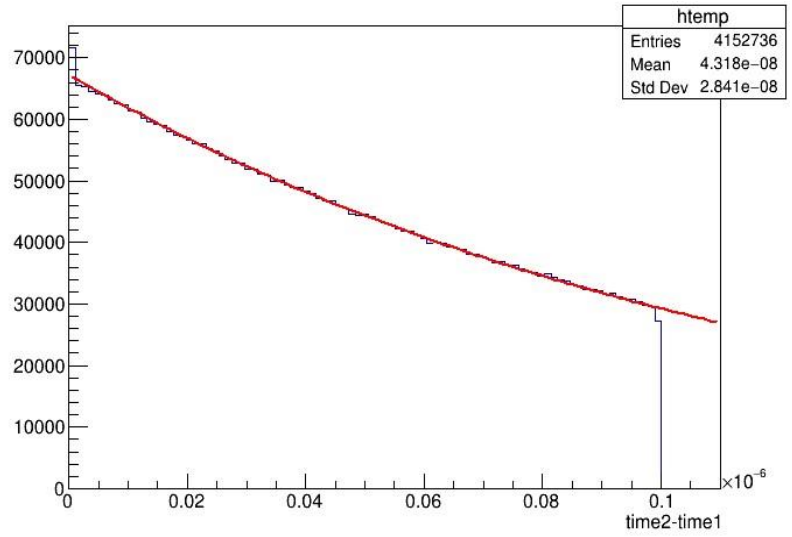

Table 2: Results of exponential fitting function

Parameter (p) name	Values	Error
Constant (p_o)	1.11159×10^{1}	8.93246×10^{-4}
Slope (p_1)	$- 8.19001 \times 10^{6}$	1.72832×10^{4}

The intermediate state lifetime between 171.3 keV and 245.4 keV is obtained by applying the data from the fitting output to the equations (02) and (03) below.

$$f(x) = \exp(p_0 + p_1 * x) \quad (02)$$

$$f(x) = N_0 * \exp\left(-t/\tau\right) \quad (03)$$

Note that, for 85 ns lifetime, τ can be computed theoretically using equation (04).

$$\tau = 85ns/\ln 2 \approx 1.226 \times 10^{-7}\,\text{s} \quad (04)$$

Where P_0 corresponds to the initial number of coincidence events**,** and P_1 corresponds to the negative decay constant (Slope obtained after applying fitting as shown in Figure 8). N_o represents the y-intercept of the fitted plot in Figure 8 (Maximum number of coincidences counts: $N_o = 67232$) and τ represent mean lifetime.

To align the fitting equations with the decay equation, a comparison between equation (02) and equation (03) was conducted. Initially, equation (02) was expanded, and subsequent parts of its equation were compared with equation (03), where by the τ from simulated data was calculated using equation (05).

$$\tau = -1/p_1 = \sim 1.221 \times 10^{-7}\,\text{s} \quad (05)$$

Now the τ value from simulated data aligns closely with the expected theoretical value 85 ns lifetime, as indicated by Equation (04). Therefore, after applying a fit to an exponential function, the measured intermediate state lifetime between 171.3 keV and 245.4 keV gamma rays emitted in the cascade decay of the indium source was found to be 84.6333 ± 0.2080 ns (computed using Equation (05)). This measured lifetime is consistent with theoretical or experimental values ranging from 84.5 ns to 85 ns [8, 18].

3.2. Coincidence event-based images

i) Image sensitivity

Figures 9 and 10 show the brightest 2D slices of an image from the 3D reconstructed position vertices of a single point source in the air and the PMMA phantom, respectively. The images were displayed in transverse, coronal, and sagittal views. The voxel bins of reconstructed images are 1.22 mm in size. The sensitivity of 22.2 cps/MBq was obtained for the ^{111}In-ion point-like source in the air at the center of FoV. For the ^{111}In-ion point-like source in the PMMA phantom at the center of FoV, the corresponding sensitivity value was 20.0 cps/MBq. The introduction of PMMA phantom naturally reduces the sensitivity by a factor of approximately 1.1 compared to a sensitivity of a point source in the air.

Figure 9: 2D-slices of an image of a single point source in the air; (a) Transverse view, (b) Coronal view, and (c) Sagittal view. The image pixel size is 1.22 mm × 1.22 mm.

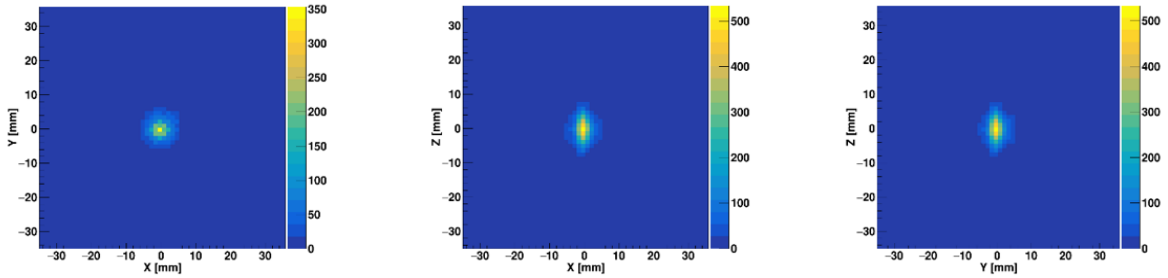

(a) (b) (c)

Figure 10: 2D-slices of an image of a single point-source in PMMA phantom; (a) Transverse view, (b) Coronal view, and (c) Sagittal view. The image pixel size is 1.22 mm × 1.22 mm.

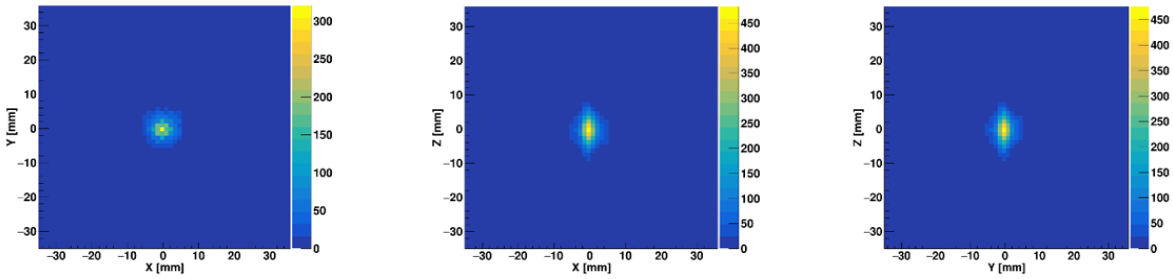

(a) (b) (c)

Results show that the imager has a system sensitivity of approximately 22.2 cps/MBq which corresponds to a coincidence detection efficiency of approximately 2.2×10^{-5} for ^{111}In source in the air at center FoV. The coincidence detection efficiency was computed as the ratio of the number of valid coincidence events in detector orientations (except for parallel

detectors) to the total number of simulated decays. Therefore, regardless of the physical geometry, simulated or prototype imaging system, the coincidence detection efficiency value from the proposed imaging modality is far better compared to previously reported imaging systems based on cascade gamma ray imaging [9].

Other previous imaging systems have reported inferior performances [33]. For instance, systems with parallel hole collimation were reported to have coincidence detection efficiency of about 6.0×10^{-8} for ^{111}In [18], 4.38×10^{-8}, and 2.51×10^{-8} for ^{111}In and ^{177}Lu, respectively [8]. While with a focused collimator, the coincidence detection efficiency of 1.6×10^{-7} for ^{111}In was reported [34]. Other coincidence imaging designs such as Compton camera and dual gamma cameras-one with a multi-slit collimator, and the other with a multi-pinhole collimator reported partial success of about 3.56×10^{-6} and 3.85×10^{-6} coincidence efficiency [20, 35]. Owing to its design, our imager is made of several detectors surrounding a source, hence a better system performance was expected.

The introduction of PMMA phantom naturally reduces the sensitivity from 22.2 cps/MBq to about 20.0 cps/MBq. The reason for this reduction is due to scattering in the phantom, which lowers the number of valid coincidence events from 40440 to 35999. This sensitivity value of about 20.0 cps/MBq (0.000020 cps/Bq) can be contrasted with the sensitivity of about 0.015 cps/Bq acquired by the same small animal PET scanner operating in a normal PET acquisition model, with a 0.25 mm diameter and approximately 400 kBq, ^{22}Na point source in a scattering medium (cubic PMMA phantom) at the center of FoV [30]. This represents a sensitivity difference of about a factor of 1:750. Therefore, from these values, it is clear that the practical use of this imaging system is challenged by the low sensitivity. However, this loss of sensitivity, which is caused by reduced geometric efficiency due to physical collimation, is overcompensated by the image reconstruction algorithm as each reconstructed decay vertex constitutes an image point, which is not an obvious case in conventional PET and SPECT imaging modalities.

ii) Spatial resolution and image size

Results obtained for spatial resolution (FWHM) of simulated point sources are presented in Table 3. The reconstructed image of a 1.0 mm diameter ^{111}In-ion point-like source in the air (Figure 9) had a spatial resolution of 4.1 mm FWHM, 4.0 mm FWHM and 7.6 mm FWHM, in the x-axis, y-axis, and z-axis, respectively. These values are similar to the spatial resolution of reconstructed images for the same point source simulated in PMMA phantom (Figure 10), which are 4.1 mm FWHM, 4.0 mm FWHM, and 7.8 mm FWHM in the x-axis, y-axis, and z-axis, respectively. Thus, it was concluded that the spatial resolution of the proposed imaging system is 4.1 mm FWHM, 4.0 mm FWHM and 7.6 mm FWHM in the x-axis, y-axis, and z-axis, respectively (Table 3).

Table 3: FWHM values (mm) for the single-point sources.

Source geometry and size (mm)	Transaxial direction		Axial direction
	x-axis (mm)	y-axis (mm)	z-axis (mm)
Diameter = 0.25	4.1	4.0	7.6
Diameter = 1.0	4.1	4.0	7.6
Diameter = 1.0 [a]	4.1	4.0	7.6
Diameter = 2.0	4.3	4.3	7.7
Diameter = 4.0	5.1 [b]	5.0 [b]	8.1
Diameter = 8.0	7.3 [b]	7.2 [b]	9.1 [b]

[a]Source in PMMA phantom.
[b]Sizes of the source were bigger than the FWHM of the imager for a particular direction, and hence the quantified sizes of images were almost the same as the sizes of the source.

As shown in Table 3, for a 0.25 mm diameter ^{111}In-ion point –like source simulated in the air at the center FoV, the spatial resolution of the imaging system in the transaxial direction was 4.1 mm FWHM in the y-axis, 4.0 mm FWHM in the x-axis, and in the axial direction was 7.6 mm FWHM. The image resolution was better in the transaxial direction than in the axial direction, because the size of the collimator hole in the transaxial is less compared to the hole size in the axial direction. The hole size usually affects the angular acceptance. Thus, with the smaller size of the hole, the narrow beam of photons is allowed to reach the detectors and hence good spatial resolution is expected. As expected, the spatial

resolution values for reconstructed images of the single ^{111}In-ion point-like source simulated in air and in the scattering medium were the same (Table 3). Therefore, it can be concluded that the scattering medium does not affect spatial resolution.

The acquired spatial resolution of 4.1 mm and 4.0 mm FWHM (in the x and y-axis), and 7.6 mm FWHM (in the z-axis) were poor compared to the spatial resolution of 2.9 mm FWHM (in the y-axis) and 2.4 mm FWHM (in the z-axis) in conventional small animal PET. The observed poor spatial resolution in the proposed imaging system might have resulted from septa penetration, geometric response, and septa scatter [36]. However, the spatial resolution from the proposed imaging system was better compared to other coincidence imaging systems. For example, coincidence imaging designs such as time-of-flight and Compton camera were reported to have a spatial resolution of 20.0 mm and 28.0 mm, respectively [19, 35].

Despite their promising figure for coincidence detection efficiency, the absence of physical collimation affected spatial resolution [19]. For collimated coincidence imaging systems, the resolution from our imager was within the reported resolutions of 6.7 to 7.0 mm for an imager with dual cameras, one with a multi-slit collimator, and the other with a multi-pinhole collimator [20]. Compared to clinical imaging systems, the resolution of our imager was better than that of clinical SPECT which ranged from 10.0-12.0 mm FWHM, and was within the reported spatial resolution of clinical PET which ranged from 5.0-7.0 mm FWHM [36].

Despite poor spatial resolution of 4.1 mm and 4.0 mm FWHM (transaxial) and 7.6 mm FWHM (axial) compared to that of a conventional small animal PET scanner, thanks to the ability of our custom image reconstruction algorithm, since with only 1,000 image points, our imager is capable of reconstructing images with sizes which are closer to the true sizes of scanned objects. However, the same phenomenon would require about 750,000 image points in conventional PET.

The relationship between the size of a scanned object (i.e., source) and FWHM can be deduced from Table 3. It was observed that if the size of the scanned object is greater or equal to 4.1 mm FWHM in transaxial (x-axis and y-axis), and greater or equal to 7.6 mm FWHM in axial (z-axis), then the size of the scanned object becomes approximately equal to the respective FWHM (mm) value. For instance, when the 8.0 mm diameter source was simulated, the spatial resolution values were 7.3 mm FWHM, 7.2 mm FWHM, and 9.1 mm FWHM in the x-axis, y-axis, and z-axis respectively. The quantified FWHM (mm) values were closer to the true diameter of the source. The observed differences in estimated image size compared to the corresponding true source size is a result of variation in FWHM value. For parallel hole collimators, the FWHM changes depending on the source position relative to the collimator hole.

iii) Resolving power

Test results for the two-point sources placed closely one to each other are presented as reconstructesd 2D images and 1D projection profiles in Figure 11 and 12. One can notice that the two sources at 7.0 mm (Figure 11 b) and 8.0 mm (Figure 11 c) distance in transaxial (x-axis) can be easily differentiated with a peak valley. In the axial direction, it can be seen that the two-ion point-like sources are partially resolved when placed at 9.0 mm distance apart center to center (Figure 12 b), and resolved when placed at 10.0 mm distance apart, center to center (Figure 12 c).

Figure 11: The 2D flattened images integrated over the Z-axis, and their corresponding 1D-projections of two ^{111}In point sources in transaxial (x-axis) direction: (a) separated 6.0 mm apart (b) separated 7.0 mm apart, and (c) separated 8.0 mm apart.

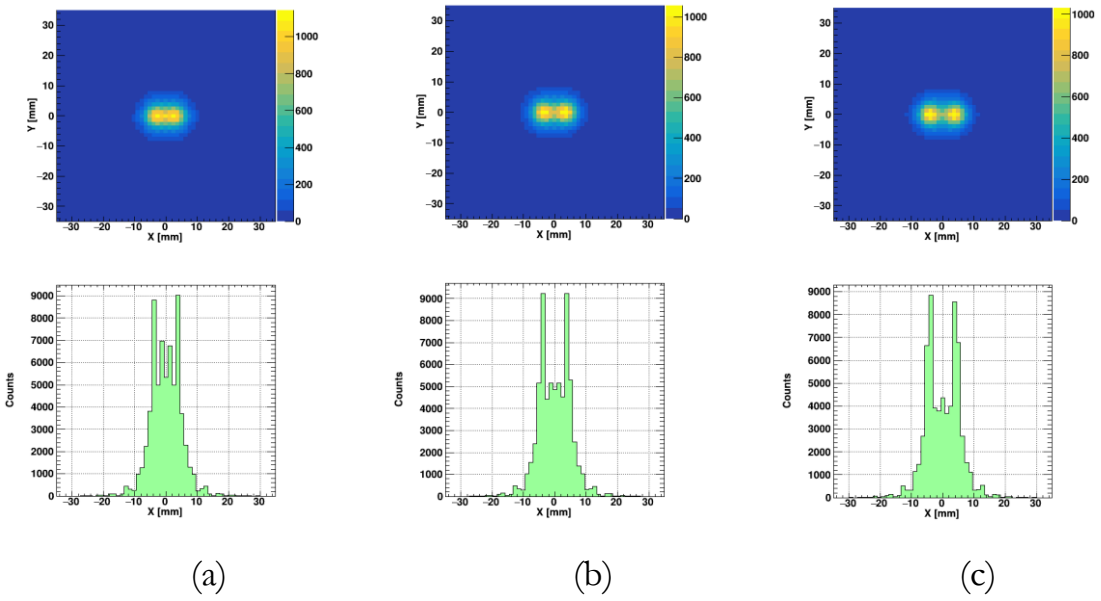

Figure 12: The 2D flattened images integrated over the Y-axis, and their corresponding 1D-projections of two ^{111}In point sources in axial (z-axis) direction: (a) separated 8.0 mm apart (b) separated 9.0 mm apart and, (c) separated 10.0 mm apart.

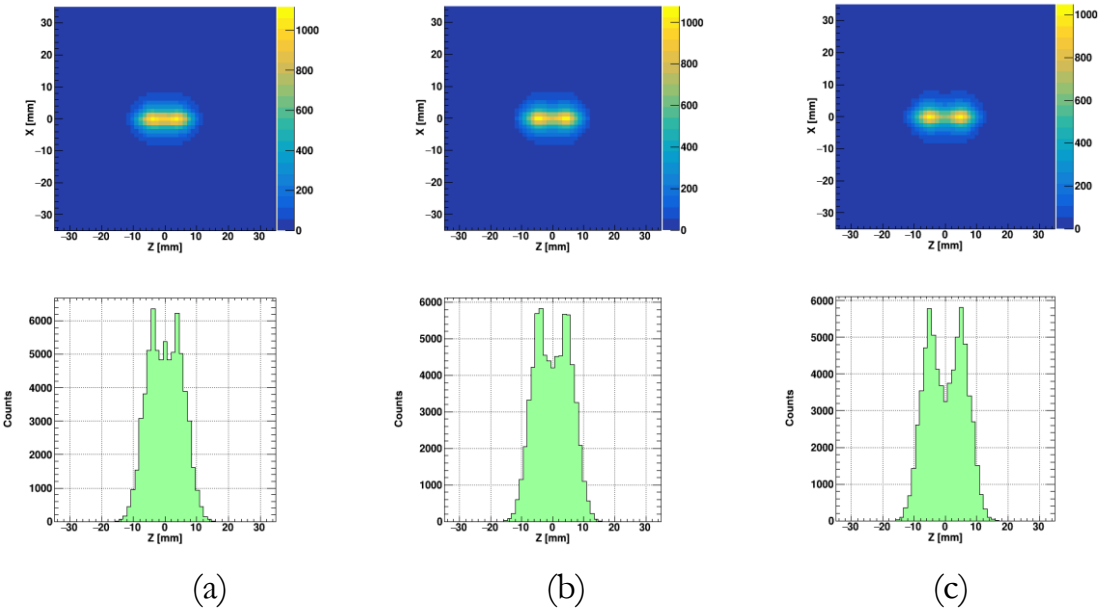

The proposed imaging system can resolve two-point sources separated 8.0 mm distance apart, center to center in transaxial (x-y plane) direction, and 10.0 mm apart, center to center in axial (z-axis) direction, respectively. For the distances below 8.0 mm and 10.0

mm in the transverse and axial directions, the presence of a background in the reconstructed image makes the source separation impossible as shown in Figure 11 and 12. The difference in system resolving power has been triggered by the differences in collimator hole size in the transaxial and axial directions. In nuclear medicine, the resolution of an imaging system is mainly dependent on several factors: the size of the detector elements, the energy of the emitted positrons, collimator hole size, and filtering applied during or post-image reconstruction. Thus, in this simulation study, collimator hole size has played a great role in estimating the image resolution and resolving power of the proposed imaging system as no filtering was applied.

4. CONCLUSIONS

This paper presents simulation results of the proposed medical imaging system using a small-animal PET scanner. Coincidence detection of non-collinear cascade gamma rays with collimated, pixelated GSO: Ce detectors showed promising performance. The method successfully localized source emission points without complex reconstruction algorithms, producing transverse, coronal, and sagittal images with minimal blurring. Future work will involve a prototype imaging experiment after fabricating and integrating the collimator system with the PET scanner.

The custom image reconstruction algorithm developed by Nkuba and Lugendo [31], used in this study, employs two collimator backprojections from valid coincidence events to estimate each decay vertex. This approach could be improved by including back-to-back (collinear) coincidences, which account for about 7.1% of valid non-collinear events. The algorithm can also be adapted for other radioisotopes with cascade gamma-ray decay, though optimizing collimator geometry for different energies remains a challenge.

The main limitation of this approach is reduced geometric efficiency compared to standard PET, due to collimator use. To address this, we propose reconstruction algorithms

that eliminate the need for collimated detectors. The current system's geometric acceptance, considering collimator losses, is about 10%, while a comparable PET system without collimators achieves roughly 30% [37]. Increasing acceptance to 30% and above would enhance data acquisition rates and image contrast.

ACKNOWLEDGMENT

We extend our sincere gratitude to Prof. Chary Rangacharyulu of the University of Saskatchewan, Canada, for welcoming us into the medical imaging group and for his valuable assistance with collimator geometry. We also thank Ms. Kaylyn Olshanoski, also from the University of Saskatchewan, for her help in configuring the collimator geometry. Our appreciation is further extended to Prof. Tomonori Fukuchi for providing the parameters of the RIKEN small-animal PET scanner used for simulation purposes. Additionally, we express our gratitude to Prof. K. Vijay Sai of the Sri Sathya Sai Institute of Higher Learning, Vidyagiri, Prasanthi Nilayam, India, for his time and expertise contributed to this study.

FUNDING

Nkuba, L.L. acknowledges the financial support from the Tanzania Atomic Energy Commission (TAEC).

CONFLICT OF INTEREST

We have no conflicts of interest to disclose.

REFERENCES

[1] RANGACHARYULU, C,; LAI THI KHANH L.Y,; OLSHANOSKI,K,; FUKUCHI, T,; FUKUDA, M,; KANDA, H,; TAKAHASHI, N. 2018 Gamma ray Angular Correlations of Nuclear Beta Decays as a Novel Medical Imaging Modality. Annual Report of RCNP of 2018, Osaka University, Ibaraki, Osaka 567-0047, Japan. https://www.rcnp.osaka-u.ac.jp/~annurep. Accessed March 18, 2021.

[2] SANTHOSH, R.S,; SHYAM, D.S,; FUKUCHI, T,; RANGACHARYULU, C,; VENKATARAMANIAH, K,; VIJAY, K.S. 2019 Design and optimization of a collimator for a New PET system using GATE simulation. Proceedings, 64th DAE BRNS Symposium on Nuclear Physics: Lucknow (Uttar Pradesh), India. 852-853.

[3] SPANOUDAKI, V.C,; LEVIN, C.S. 2010 Photo-detectors for time-of-flight positron emission tomography (ToF-PET). Sensors. 10(11) 10484-10505.

[4] KWON, S.I,; OTA, R,; BERG, E,; HASHIMOTO, F,; NAKAJIMA, K,; OGAWA, I,; TAMAGAWA, T,; OMURA, T,; HASENGWA, T,; CHERRY, S.R. 2021 Ultrafast timing enables reconstruction-free positron emission imaging. Nature Photonics. 15 914-918.

[5] DAS, P,; VERMA, R,; PRASAD, K. 2024 Exploring PET imaging with scattered photons and polarization characteristics, Bio-Algorithms and Med-Systems. 20 (special issue) 10-16, DOI: 10.5604/01.3001.0054.8576.

[6] CONTI, M,; BENDRIEM, B. 2019 The new opportunities for high time resolution clinical TOF PET. Clin. Trans. Imaging. 7 139-147.

[7] SHIMAZOE, K,; UENOMACHI, M,; MIZUMACHI, Y,; TAKAHASHI, H,; MASAO, Y,; SHOJI, Y,; KAMADA, K,; YOSHIKAWA, A. 2017 Double Photon Emission Coincidence Imaging using GAGG-SiPM pixel detectors. JINST (11th Int. Conference on Position Sensitive Detectors). 12 C12055.

[8] UENOMACHI, M,; SHIMAZOE, K,; OGANE, K,; TAKAHASHI, H. 2021 Simultaneous multi-nuclide imaging via double-photon coincidence method with parallel hole collimators. Nature-Portfolio Sci Rep 11 13330.

[9] NKUBA, L.L. 2024 Design and Development of a Non-Collinear Gamma Cascade Correlation Based Medical Imaging System. Unpublished PhD in Physics (Thesis), University of Dar es Salaam, Tanzania.

[10] RANGACHARYULU,C,; LAI THI KHANH L.Y,; OLSHANOSKI, K,; SANTOSH, S,; NKUBA, L.L,; FUKUCHI, T,; FUKUDA, M,; KANDA, H,; MSAKI, P.K,; SAI, K.V,; TAKAHASHI, N. 2020 Development of a Nuclear Gamma Cascade

Correlations Based Medical Imaging System - A Novel Modality with Potentials for Replacement of SPECT and PET. International Conference on Clinical PET-CT and Molecular Imaging in the Era of Theranostics (IPET-2020). Book of Abstract-IPT 2020. IAEA-CN-285/110.

[11] UENOMACHI, M,; SHIMAZOE, K,; TAKAHASHI, H. 2022 A double photon coincidence detection method for medical gamma-ray imaging. Bio-Algorithms and Med-Systems. 18(1) 120-126. https://doi.org/10.2478/bioal-2022-0080.

[12] SHIMAZOE, K,; UENOMACHI, M. 2022 Multi-molecule imaging and inter-molecular imaging in nuclear medicine, Bio-Algorithms and Med-Systems. 18(1) 127-134 https://doi.org/10.2478/bioal-2022-0081.

[13] SCHMITZ-FEUERHAKE, I. 1970 Studies on three-dimensional scintigraphy with gamma-gamma coincidence. Phys Med Biol. 15(4) 649-656.

[14] POWELL, M.D,; MONAHAN, W.G. 1972 Three-Dimensional Radionuclide Imaging. Phys. Med. Biol. 17(6) 867-872.

[15] HART, H.E,; RUDIN, S. 1977 Three-Dimensional Imaging of Multimillimeter Sized Cold Lesions by Focusing Collimator Coincidence Scanning. IEEE Transactions on Biomedical Engineering. 24(2) 169-177.

[16] VON BOETTICHER, H,; HELMERS, H,; MUSCHOL, E.M. 1979 Contributions to depth discrimination γ-γ-coincidence methods in scintigraphy. Phys. Med. Biol. 24(3) 571-576.

[17] HELMERS, H,; VON BOETTICHER, H,; SCHMITZ-FEUERHAKE, I. 1979 Scanner Performance to Overcome Efficiency Problems in Three-dimensional Scintigraphy by γ-γ-coincidences. Phys. Med. Biol. 24(5) 1025-1029.

[18] PAHLKA, R.B,; KAPPADATH, S.C,; MAWLAW, O.R. 2018 A Monte Carlo simulation of coincidence detection and imaging of gamma-ray cascades with a scintillation camera. Biomed. Phys. Eng. Express. 4 055012.

[19] CHIANG, C.C,; CHUANG, C.C,; NI, Y.C,; JAN, M.L,; CHUANG, K.S,; LIN, H.H. 2020 Time of flight dual photon emission computed tomography. Sci Rep 10 19514.

[20] LIU, X,; LIU, H,; CHENG, L,; WU, J,; BAO, T,; YAO, ,; LIU, Y. 2021 A 3-dimensional stationary cascade gamma-ray coincidence imager. Phys. Med. Biol. 66 225001.

[21] BRADY, E.L,; DEUTSCH, M. 1950 Angular correlation of successive gamma rays. Phys. Rev. 78(5) 558–566.

[22] BÉ, M.M,; CHISTÉ, V,; DULIEU, C,; BROWNE, E,; BAGLIN, C,; CHECHEV, V,; KUZMENKO, N,; HELMER, R.L,; KONDEV, F,; MACMAHON, T.D,; LEE, K.B. 2006 Table of radionuclides (Vol. 3 – A = 3 to 244). Bureau International des Poids et Mesures 5. Table of radionuclides. 92-822-2218-7 Available online at https://inria.hal.science/cea-02476243/ Retrived on March 25, 2023.

[23] SEABOLD, J.E,; FORSTROM, L.A,; SCHAUWECKER, D.S,; BROWN, M.L,; DATZ, F.L,; MCAFEE, J.G,; PALESTRO, C.J,; ROYAL, H.D. 1997 Procedure guideline for indium-111-leukocyte scintigraphy for suspected infection/inflammation. Society of Nuclear Medicine. J Nucl Med. 38(6) 997-1001.

[24] KHALIL, M.M,; TREMOLEDA, J.L,; BAYOMY, T.B,; GSELL, W. 2011 Molecular SPECT imaging: an overview. Int. J. Mol. Imaging. 796025, page 1-15.

[25] JAN, S,; BENOIT, D,; BECHEV,A.E,; LIN, H,; CHUANG, K,; LIN, Y,; PET, C,; ESPAÑA, S,; HERRAIZ, J.L,; VICENTE,E,; LAZARO, D,; BUVAT, I,; LOUDOS, G. 2004 GATE : a simulation toolkit for PET and SPECT. Phys. Med. Biol. 49(19): 4543–4561.

[26] BRUN, R,; RADEMAKERS, F. 1997 ROOT - An object oriented data analysis framework Nucl. Instruments Methods Phys. Res. Sect. A Accel. Spectrometers, Detect. Assoc. Equip. 389 81–86.

[27] OKUMURA,S,; YAMAMOTO, S,; WATABE, H,; KATO, N,; HAMAMURA, H. 2015 Development of dual layer GSO depth-of-interaction block detector using angled optical fiber. Nucl. Instr. and Meth. in Phys. Res. A781 65-70.

[28] YAMAMOTO, S,; OKUMURA, S,; WATABE, T,; IKEDA,H,; KANAI,Y,; TOSHITO, T,; KOMORI, M,; OGATA, Y,; KATO, K,; HATAZAWA, J. 2015 Development of a prototype Open-close positron emission tomography system. Rev. Sci. Instrum. 86 084301.

[29] FUKUCHI, T,; OKAUCHI, T,; SHIGETA, M,; YAMAMOTO, S,; WATANABE, Y,; ENOMOTO, S. 2017 Positron emission tomography with additional γ-ray detectors for multiple-tracer imaging. Med. Phys. 44(6) 2257-2266.

[30] NKUBA, L.L,; LUGENDO, I.J,; AMOUR, I.S. 2021 A GATE-based Monte Carlo simulation of a dual-layer pixelized gadolinium oxyorthosilicate (GSO) detector performance and response for micro-PET scanner. Tanzania Journal of Science. 47(2) 507-519.

[31] NKUBA, L.L,; LUGENDO, I.J. 2025 A Monte Carlo Simulation Study on the Design and Optimization of Collimators for Non-Collinear Cascade Gamma-Ray Correlation

Emissions in Medical Imaging. Brazilian Journal of Radiation Sciences. 13(1) 01-31. Doi: 10.15392/2319-0612.2025.25732025.

[32] MATULEWICZ, T,; KORZECKA, K,; PYTEL, Z. 1996 Tests of GSO scintillator In: Annual Reports: Nuclear Physics Division, Insititute of Experimental Physics. Warsaw University (Eds S. Zygmunt & M. Popkiewicz), PL9800110. 48–49.

[33] NKUBA, L.L,; JUNIOR, I.J,; MOHAMED, S.M,; LUGENDO, I.J,; MOHAMMED, N.K. 2022 Review of the Imaging Performance and the Current Status of the Cascade Gamma-Rays Coincidence Imagers Tanzania J. Enrg. Technol. 41(4) 229–246

[34] CHOGHADI, M.A,; KITAJIMA, M,; UENOMACHI, M,; SHIMAZOE, K,; TAKAHASHI, H. 2021 Collimator-based Coincidence Imaging for Double Photon Emitting Nuclides. Radioisotopes. 70(4) 271–277.

[35] YOSHIHARA,Y,; SHIMAZOE, K,; MIZUMACHI, Y,. TAKAHASHI, H. 2017 Evaluation of double photon coincidence Compton imaging method with GEANT4 simulation. Nuclear Inst. and Meth. in Phy. Res. A 873 51–55.

[36] PRIOR, J.O,; LECOQ, P. 2012 Radiation-Based Medical Imaging Techniques: An Overview. In "Handbook of Particle Detection and Imaging" Edited by Grupen C, Buvat I. Springer-Verlag Berlin Heidelberg; 862 p.

[37] OLSHANOSKI, K,; NKUBA, L.L,; DANG, N.P,; FUKUCHI, T,; KANDA, H,; LUGENDO, I.J,; VIJAY, SAI.K,; RANGACHARYULU, C. 2023 Collimator design for gamma-ray cascade angular correlations in medical imaging, Vol. 18, no. 5, p. C05010. Publisher: IOP Publishing.

LICENSE